Available online at www.sciencedirect.com

SciVerse ScienceDirect

Acta Materialia 60 (2012) 6621–6630

Acta MATERIALIA

www.elsevier.com/locate/actamat

Finite-element modelling of heat transfer in shaped metal deposition and experimental validation

Víctor D. Fachinotti [a,*], Alberto Cardona [a], Bernd Baufeld [b], Omer Van der Biest [b]

[a] Centro Internacional de Métodos Computacionales en Ingeniería (CIMEC-INTEC), Universidad Nacional del Litoral (UNL)/ Consejo Nacional de Investigaciones Científicas y Técnicas (CONICET), Predio CCT-CONICET Santa Fe, Colectora Ruta Nacional 168, Paraje El Pozo, 3000 Santa Fe, Argentina

[b] Department of Metallurgy and Materials Engineering (MTM), Katholieke Universiteit Leuven (KUL), Kasteelpark Arenberg 44, 3001 Leuven, Belgium

Received 18 May 2012; received in revised form 10 August 2012; accepted 15 August 2012
Available online 18 September 2012

Abstract

Shaped metal deposition (SMD) is a novel technology for building near-net-shaped components by successive layer deposition using a welding machine. The SMD rig consists of a robot with a tungsten inert gas welding torch and manipulator, both of which are housed inside a sealed chamber. A series of walls were made from Ti–6Al–4V alloy by SMD and the heat transfer problem during layer deposition was analysed in all cases. The specimens were built using a wide range of process parameters (number of layers, layer height, wire feed rate, travel speed, heat input, etc.) and wall dimensions. During the fabrication process, the SMD built part is subjected repeatedly to high temperature gradients and high heating and cooling rates, resulting in a unique morphology and microstructures usually not observed in conventional fabrication techniques. A finite-element model for the thermal analysis of this deposition process was constructed. The aims of this study are, firstly, to correlate the predicted temperature field to experimental observations to validate the numerical model of this complex process; and secondly, to explain on the basis of the computed temperature and temperature rate the appearance of characteristic microstructures on the top of the walls, and in the substrate and intermediate region.

Keywords: Shaped metal deposition; Finite elements; Temperature evolution; Microstructure

1. Introduction

Shaped metal deposition (SMD) is a near-net-shape rapid prototyping system patented by Rolls-Royce plc [1]. It is particularly useful to the aerospace industry for building components out of titanium alloys. This study deals with deposition of Ti–6Al–4V alloy, which is of great interest to builders of aerospace components. The SMD rig consists of a robot with a tungsten inert gas (TIG) welding head housed within a sealed chamber filled with argon. The gas purity in the chamber is 99.999% to prevent the substrate, electrode and component from reacting with atmospheric gases.

SMD allows a complex component to be built directly from its computer-aided design (CAD) model with minimum finishing operations. The welding robot creates the component from the base up in a layer-wise fashion, depositing material along the CAD-dictated path without the need for support structures. The temperature field developed during SMD is a function of many welding parameters, such as the arc power, welding speed, welding sequences and environmental conditions [2]. The accuracy in the component depends on the thermal stresses induced during the welding process. The appropriate control of heat transfer during material deposition reduces residual stresses and hence component distortion. Process parameters that give rise to successfully manufactured components

* Corresponding author. Tel.: +54 342 4511594; fax: +54 342 4511169.
E-mail addresses: vfachino@intec.unl.edu.ar (V.D. Fachinotti), acardona@intec.unl.edu.ar (A. Cardona), B.Baufeld@namrc.co.uk (B. Baufeld), Omer.VanderBiest@mtm.kuleuven.be (O. Van der Biest).

1359-6454/$36.00
http://dx.doi.org/10.1016/j.actamat.2012.08.031

are usually determined experimentally by trial and error, a very costly and time-consuming procedure.

Computational welding mechanics (CWM) is an alternative for determining the influence of process parameters on heat transfer during welding processes [3,4]. Heat transfer in CWM is modelled by a strongly non-linear partial differential equation that has to be solved at each time step until the end of the process. The use of an explicit time-step scheme is discouraged for phase-change heat transfer equations [5–8]; therefore, the heat transfer equation must be solved iteratively at each time step. A robust phase-change model should be used to ensure the convergence of the iterative solution at each computation step [9].

SMD poses several particular challenges to CWM. On the one hand, to model the moving welding heat source accurately, the source traversing through any cross-section to the welding path should be made in several time steps. Taking into account the typical source dimensions and travel speeds, this requires time steps as small as 0.1seconds. On the other hand, a typical component usually consists of tens to hundreds of deposited layers, so the simulation should span up to several hours with a very small time step in order to predict the final state of the component.

Concerning spatial discretization, the modelling of the temperature gradient across the thickness of the last deposited layers requires a fine mesh in the thickness direction. Together with the large number of required time steps, this prevents the use of a three-dimensional (3-D) model for SMD. In fact, most of the numerical 3-D models of metal deposition processes available in the literature [10–14] assume a simplified rectangular geometry for the cross-section of each layer and the mesh refinement along the layer thickness is not enough to ascertain the steep temperature variation in the last deposited layers. The 3-D finite-element model of SMD developed by Anca et al. [15], in which the geometry of each layer is properly described, restricted the analysis to the deposition of only four layers with a poor mesh refinement along the thickness of the deposited layers. Most of these 3-D models were, however, focused on the determination of the distortion of the component giving satisfactory results when compared to experiments.

Therefore, the high computational cost of transient 3-D models makes 2-D simplified models very popular for heat-transfer analysis in metal deposition. Hence, a 2-D cross-sectional model is generally used and a typical section normal to the deposition path is analysed. In a previous paper, we demonstrated the satisfactory behaviour of 2-D cross-sectional models in comparison to full 3-D models for the analysis of the heat transfer induced by an SMD welding heat source [16]. Similar conclusions are found in previous works on thermal analysis of welding processes [17–20]. Recently, Barsoum and Lundbäck [21] remarked that 2-D models with dense meshes resolve the heat-affected zone (HAZ) and the fusion zone (FZ) better than do 3-D models, for which the use of dense meshes is presently uneconomical. This is in accordance with the observations by Lindgren [22], who stated that 3-D models remain too computer-intensive to be accurate for multipass welding.

Kelly [23] and Kelly and Kampe [24] created a 2-D cross-section model for laser deposition of Ti–6Al–4V, using the finite-difference method to discretize the spatial domain. They assumed a rectangular cross-section for each layer, probably because of the lack of versatility of the finite-difference method for representing non-rectangular geometries. Additionally, Charles and Järvstråt [25] used the 2-D cross-section model for heat transfer analysis in a process similar to SMD. In this case, the finite-element method was used and the geometry of the cross-section of each layer was properly represented. Further, an adequately dense mesh was observed. Unfortunately, this work focused on the prediction of microstructure and did not include additional details on the thermal model.

The present work develops a complete model for the determination of the thermal field along the entire SMD process, including the so-called TIG-wash steps consisting of passes of the welding torch without filling material to pre-heat the substrate before deposition. The analysis is extended until the temperature of the entire component becomes low enough to ensure that the material does not suffer additional microstructural changes. The model is used to study the influence of the main process parameters on the thermal field, specifically on the prediction of the top cupola of deposited Ti–6Al–4V walls where a steep change in microstructure is observed [26,2].

The classical double-ellipsoidal welding heat source model [27] is used to represent the TIG-wash steps and the deposition of the first layer, as is usually performed in the literature for welding without filler material or a single-pass welding. Based on observations of the shape of the liquid pool on subsequent layers, the double-ellipsoidal heat source model is replaced by a constant heat power density throughout the newly added material and the thermal conductivity is increased artificially, as is usually performed for modelling improved heat transfer by convection. Additionally, based on observations, and unique to this model, we assume that the melt flowing onto the previously deposited material is the preferred heat carrier and, consequently, the conductivity should be increased mainly in this direction. Both improvements contribute to the optimal modelling of the liquid pool using a heat conduction model, i.e. without the high cost of modelling the melt flow.

The results of this model, i.e. the temperature history at each point of the entire component along the SMD process, allows us to explain important microstructural features, such as the top cupola, whose microstructure differs considerably from that of the lower layers, as well as the absence of martensite, contrary to the results reported in the literature for TIG-welding of Ti–6Al–4V using techniques such as spot welding [28] and pulsed-current welding [29,30]. In fact, although high cooling rates are observed during the deposition of the first layers (as observed for one-pass welding), this zone is reheated by

the deposition of the subsequent layers and the martensite that could be formed during these early stages is completely dissolved. In the final layers, which do not suffer reheating, the cooling rate is less than that of the first layers, which may explain the absence of martensite.

2. SMD test specimens

Fig. 1 shows a sample component of Ti–6Al–4V alloy made by SMD with the shape addressed in this work: square tubes with different dimensions built by varying the main process parameters (arc current and voltage, welding speed, wire feed rate, number of layers) over a wide range, as shown in Table 1.

Fig. 2 depicts etched cross-sections of optical macrographs taken from the walls of the parts selected for this study. In all of them, we can distinguish a top region with fine α lamellae within a β matrix, as well as a bottom region characterized by the presence of bands parallel to the base with coarser α phase lamellae. The top region represents the area where the peak temperature exceeded the β-transus temperature T_β during the last pass [26]. In other words, this top region embodies the FZ consisting of the material whose peak temperature has exceeded the solidus temperature T_S plus the HAZ where the maximal temperature ranges between T_β and T_S.

Prediction of this region is one of the main objectives of the present work. To this end, the evolution of temperatures within the domain consisting of the base plate (also Ti–6Al–4V in this case) and the wall, which grows gradually layer by layer along the deposition process, will be computed.

3. Heat transfer problem in SMD

The problem to be solved is written as follows: find the temperature field $T = T(x,y,t)$ at any point $(x,y) \in \Omega(t)$ and for any time instant $t \in (t_0, t_F]$ that satisfies the transient heat conduction equation:

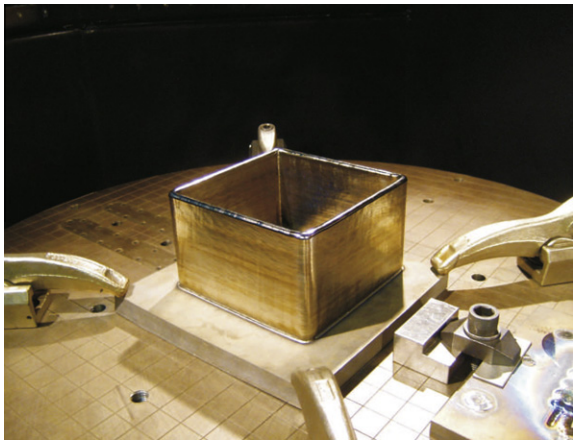

Fig. 1. Square cylinder produced by SMD.

Table 1
Geometrical data and process parameters used to build the selected samples.

Sample	21	22	23	24	35	50
Thickness [mm]	9.45	9.49	8.75	9.87	9.67	19.80
Side length [mm]	140	140	140	140	140	100
Total height [mm]	70	70	70	70	70	25
Number of TIG-wash passes	3	3	3	3	3	6
Number of layers	70	87	87	70	70	50
Current during TIG-wash [A]	140	140	140	140	140	130
Current during deposition [A]	182.5	164.7	163.4	183.2	182.5	221.4
Current [A]	182.5	164.7	163.4	183.2	182.5	221.4
Voltage [V]	12.8	11.2	11.6	12.4	12.8	11.5
Wire feed rate [mm min^{-1}]	2200	1400	1800	2400	2200	770
Welding velocity [mm min^{-1}]	250	250	300	300	300	100

$$\frac{\partial H}{\partial t} - \operatorname{div}(\mathbf{k}\ \operatorname{grad}\ T) = q \qquad \forall (x,y) \in \Omega(t), \tag{1}$$

where $H = H(T)$ is the enthalpy, $\mathbf{k} = \mathbf{k}(T)$ is the thermal conductivity tensor and $q = q(x,y,t)$ is the heat source (in our case the welding torch). The domain $\Omega(t)$ is evolving in time because of the material deposition. The problem definition is completed by the initial condition:

$$T(x,y,t_0) = T_0(x,y) \qquad \forall (x,y) \in \Omega(t_0), \tag{2}$$

the adiabatic (natural) boundary condition at the symmetry axis:

$$\operatorname{grad} T \cdot \mathbf{n} = 0 \qquad \forall (x,y) \in \Gamma^{\mathrm{sym}}(t),\ t_0 < t < t_F, \tag{3}$$

and the convection/radiation (mixed) boundary condition:

$$-\mathbf{k}\ \operatorname{grad} T \cdot \mathbf{n} = h_{\mathrm{cr}}(T - T_{\mathrm{cr}}) \quad \forall (x,y) \in \Gamma^{\mathrm{cr}}(t),\ t_0 < t < t_F, \tag{4}$$

where $\mathbf{n}$ is the unit vector normal to the boundary and pointing outwards, $h_{\mathrm{cr}} = h_{\mathrm{cr}}(T)$ is the convection/radiation coefficient, T_{cr} is either the temperature of the surrounding fluid or that of the radiant body, and t_0 and t_F are, respectively, the initial and final time of analysis.

The initial temperature $T_0(x,y)$ is taken to be equal to room temperature. The filler material entering the domain is also considered to be equal to room temperature, and the welding heat source must be powerful enough to heat and melt this material. In other words, we adopt T_0 equal to room temperature both for the substrate as well as for the layers entering the domain. This hypothesis is different from that used by other authors [10,21,13], who consider the material in deposited layers to be initially at melting temperature.

A temperature-based formulation is recovered by defining the enthalpy function as follows:

$$H(T) = \int_0^T \rho c_p\ \mathrm{d}V + \rho L f_{\mathrm{L}}(T) \tag{5}$$

where $\rho c_p(T)$ is the heat capacity, ρL is the latent heat of solidification and $f_{\mathrm{L}}(T)$ is the liquid volume fraction.

Following Rai et al. [31] and Kelly [32], the liquid fraction for Ti–6Al–4V is assumed to vary linearly with

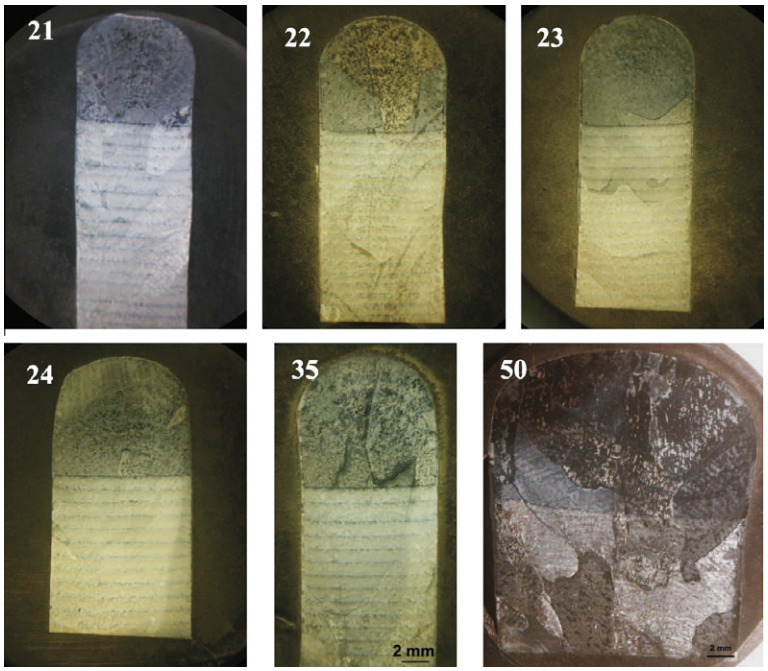

Fig. 2. Optical macrographs of cross-sections of selected walls made by SMD (pictures do not have the same scale).

temperature from the solidus temperature T_S to the liquidus temperature T_L, i.e.:

$$f_L = \begin{cases} 0 & \text{if } T \leqslant T_S \\ \frac{T-T_S}{T_L-T_S} & \text{if } T_S < T < T_L \\ 1 & \text{if } T \geqslant T_L \end{cases} \tag{6}$$

The latent heat in solid-phase transformations is assumed to be negligible compared to the latent heat of fusion in Ti–6Al–4V [33].

Convection effects increase heat transfer within the weld pool. This effect is modelled by adopting an artificially increased conductivity for the molten metal equal to 1.5–10 times the value of the liquid at rest [34–39,33,40]. Some authors propose using an orthotropic conductivity in the weld pool; Askari et al. [41] used an orthotropic conductivity with a higher value along the pool depth to represent convection effects. In our case, the shape of the FZ in SMD walls (Fig. 5) suggests that the conductivity must be increased mainly in the direction tangential to the top surface of the wall to account for the molten metal pouring effects (see Section 5.2).

4. Finite-element modelling

The finite-element formulation for the solution of the heat conduction equation with phase change has been introduced elsewhere [9]. A brief description is included here for the sake of completeness.

The time interval of analysis is discretized in a series of time instants $t_I \in [t_0, t_F], I = 0,1,2,\ldots N$. At each time instant t_I, a domain $\Omega_I = \Omega(t_I)$ is considered, which is assumed frozen during the interval $[t_I, t_{I+1})$. The weak form of the heat conduction problem, i.e. the initial and boundary value problem defined by Eqs. (1)–(5) and supplemented by the constitutive law for enthalpy (Eq. (5)), can then be written as follows: find $T \in \mathcal{V}$ such that

$$\begin{aligned} &\int_{\Omega_I} \rho c_P \frac{\partial T}{\partial t} w \, \mathrm{d}V + \int_{\Omega_I} \mathbf{k} \, \mathrm{grad}\, T \cdot \mathrm{grad}\, w \, \mathrm{d}V \\ &\quad + \int_{\Gamma_I^{cr}} h_{cr}(T - T_{cr}) w \, \mathrm{d}V + \frac{\partial}{\partial t} \int_{\Omega_I} \rho L f_L w \, \mathrm{d}V \\ &\quad = \int_{\Omega_I} q w \, \mathrm{d}V, \qquad I = 1,2,\ldots N \end{aligned} \tag{7}$$

for all admissible weighting functions $w \in \mathcal{V}$. The finite-element space $\mathcal{V}$ is built with linearly interpolated triangular elements covering the domain Ω_I. The finite-element approximation for the temperature field can be written as:

$$T(x,y,t) = \sum_{j=1}^{n^n} N_j(x,y) T_j(t) \tag{8}$$

where $T_j(t)$ is the temperature at node j, $N_j(x,y)$ is the shape function associated with this node and n^n is the number of nodes. The standard (Galerkin) finite-element formulation assumes further that the weight functions coincide with the shape functions, yielding:

$$\begin{aligned} &\underbrace{\int_{\Omega_I} \rho c_P N_i N_j \, \mathrm{d}V}_{C_{ij}^I} \frac{\mathrm{d}T_j}{\mathrm{d}t} + \underbrace{\int_{\Omega_I} \mathbf{k} \, \mathrm{grad}\, N_i \cdot \mathrm{grad}\, N_j \, \mathrm{d}V}_{K_{ij}^I} T_j \\ &\quad + \frac{\partial}{\partial t} \underbrace{\int_{\Omega_I} \rho L f_L N_i \, \mathrm{d}V}_{L_i^I} = \underbrace{\int_{\Omega_I} q N_i \, \mathrm{d}V}_{F_i^{I;\mathrm{whs}}} - \underbrace{\int_{\Gamma_I^{cr}} h_{cr} N_i (N_j T_j - T_{cr}) \, \mathrm{d}V}_{F_i^{I;\mathrm{cr}}} \end{aligned} \tag{9}$$

where C_{ij}^I is the capacitance (or mass) matrix, K_{ij}^I is the conductivity (or stiffness) matrix, L_i^I is the latent heat vector,

$F_i^{I;\mathrm{whs}}$ is the welding heat source vector and $F_i^{I;\mathrm{cr}}$ is the convection-radiation heat flux vector.

The capacitance and stiffness matrices and the heat flux vector are the usual ones in thermal finite-element analysis and their computation is given in many texts (see e.g. [42]). The treatment of the welding heat source is detailed in Section 5.

The latent heat vector is evaluated using the discontinuous integration technique proposed by Fachinotti et al. [9]. Let Ω^e be a linear triangular finite-element affected by phase change and containing a solid subdomain Ω^e_{S}, a mushy subdomain Ω^e_{M}, and a liquid subdomain Ω^e_{L}, i.e. $\Omega^e = \Omega^e_{\mathrm{S}} \cup \Omega^e_{\mathrm{M}} \cup \Omega^e_{\mathrm{L}}$. These sub-regions are easily identified because the temperature field is linearly interpolated. The element integral is then computed as the sum of integrals over each subdomain, within which the integrand varies smoothly. The contribution to the latent heat vector of an element Ω^e affected by phase change is therefore computed as:

$$L_i^e = \int_{\Omega^e} \rho L f_{\mathrm{L}} N_i \, \mathrm{d}V = \rho L \int_{\Omega^e_{\mathrm{L}}} N_i \, \mathrm{d}V + \rho L \int_{\Omega^e_{\mathrm{M}}} N_i \frac{N_j T_j - T_{\mathrm{S}}}{T_{\mathrm{L}} - T_{\mathrm{S}}} \, \mathrm{d}V \tag{10}$$

Conductivity exhibits a jump across the solidification interval when it is artificially increased to model the convection effects within the weld pool. Hence, it deserves a treatment similar to that of latent heat. The bulk or effective conductivity is defined as follows:

$$\mathbf{k}(T) = \mathbf{k}_{\mathrm{m}}(T) + f_{\mathrm{L}}(T)\Delta\mathbf{k}(T) \tag{11}$$

where $\mathbf{k}_{\mathrm{m}}$ denotes molecular conductivity, which coincides with that of the liquid at rest for $T > T_{\mathrm{L}}$, and $\Delta\mathbf{k}$ is the artificial increment for convection effects. The effective conductivity is typically 1.5–10 times the molecular conductivity and is generally orthotropic. The element conductivity matrix is then computed as follows:

$$K_{ij}^e = \int_{\Omega^e} \mathbf{k}_{\mathrm{m}} \, \mathrm{grad}\, N_i \cdot \, \mathrm{grad}\, N_j \, \mathrm{d}V + \int_{\Omega^e_{\mathrm{M}}} f_{\mathrm{L}} \Delta\mathbf{k} \, \mathrm{grad}\, N_i \cdot \, \mathrm{grad}\, N_j \, \mathrm{d}V + \int_{\Omega^e_{\mathrm{L}}} \Delta\mathbf{k} \, \mathrm{grad}\, N_i \cdot \, \mathrm{grad}\, N_j \, \mathrm{d}V \tag{12}$$

The treatment of the artificial increment $\Delta\mathbf{k}$ is further discussed in Section 5.1.

4.1. Time integration

The fully implicit and unconditionally stable Euler-backward scheme is used for time integration: once $T^{I-1} = T(t_{I-1})$ is known, $T^I = T(t_I)$ is determined by solving the following system of non-linear algebraic equations:

$$C_{ij}^I \frac{T_j^I - T_j^{I-1}}{\Delta t} + K_{ij}^I T_j^I + \frac{L_i^I - L_i^{I-1}}{\Delta t} = F_i^{I;\mathrm{whs}} + F_i^{I;\mathrm{cr}} \tag{13}$$

where the super-indices $I-1$ and I denote evaluation at times t_{I-1} and t_I, respectively, and $\Delta t = t_I - t_{I-1}$ is the time step.

Eq. (13) is highly non-linear, mainly due to the latent heat term and the jump in conductivity from modelling the convection effects. An exact Newton–Raphson technique is used to efficiently solve it. The computation of the tangent matrix is detailed in a previous work [9].

5. Arc-welding heat source model

The arc-welding heat source is described using the double-ellipsoidal model proposed by Goldak et al. [27] and shown in Fig. 3. The heat input rate density per unit volume is:

$$q^{\mathrm{Goldak}}(x',y',z') = \frac{6\sqrt{3}Q}{\pi\sqrt{\pi}ab} \times \begin{cases} \frac{f_f}{c_f} \exp\left(-3\frac{x'^2}{a^2} - 3\frac{y'^2}{b^2} - 3\frac{z'^2}{c_f^2}\right) & \text{if } z' > 0 \\ \frac{f_r}{c_r} \exp\left(-3\frac{x'^2}{a^2} - 3\frac{y'^2}{b^2} - 3\frac{z'^2}{c_r^2}\right) & \text{if } z' < 0. \end{cases} \tag{14}$$

where Q is the total heat input, O'-$x'y'z'$ is a moving orthogonal system of coordinates (with origin O' coinciding with the trace of the torch onto the surface of the weld, the z'-axis pointing along the welding direction, the x'-axis lying on the weld surface and the y'-axis defining the depth), a, b, c_f (or c_r) are the semi-axes of the front (or rear) semi-ellipsoid, f_f (or f_r) is the portion of heat distributed in the front (or rear) semi-ellipsoid, with $f_f + f_r = 2$. Following Nguyen et al. [43], we adopt $f_f/c_f = f_r/c_r$ to guarantee the continuity of $q(x',y',z')$ at $z' = 0$.

In the 2-D model, the heat flow along the z direction is assumed negligible, i.e. $\frac{\partial T}{\partial z} = 0$, and the analysis is focused on a given cross-section at $z = 0$. This hypothesis is valid for large Pclet numbers [44,3], defined as:

$$Pe = \frac{V_w l}{\kappa} \tag{15}$$

where V_w is the welding speed (see Table 1), l is a characteristic dimension in the welding direction and κ is the thermal diffusivity.

Let $z(t)$ be the position of the welding torch relative to the section of analysis such that $z < 0$ (or $z > 0$) before

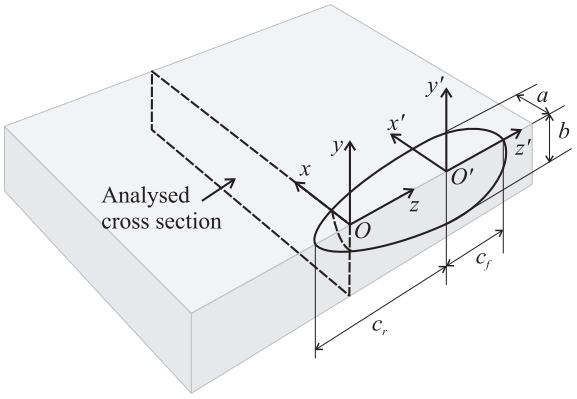

Fig. 3. Double-ellipsoidal heat source [27].

(or after) the torch passes through this section; also, let $x \equiv x'$ and $y \equiv y'$, as shown in Fig. 3. Note that $z = -z'$ for all points within the section of analysis. The heat input density per unit area at a point $(x,y) \in \Omega \equiv \Omega_0$ (i.e. within the substrate) and at any time instant before deposition of the first layer is:

$$q(x,y,t) = \frac{6\sqrt{3}Q}{\pi\sqrt{\pi}ab} \times \begin{cases} \frac{f_f}{c_f}\exp\left(-3\frac{x^2}{a^2}-3\frac{y^2}{b^2}-3\frac{z(t)^2}{c_f^2}\right) & \text{if } z(t)<0 \\ \frac{f_r}{c_r}\exp\left(-3\frac{x^2}{a^2}-3\frac{y^2}{b^2}-3\frac{z(t)^2}{c_r^2}\right) & \text{if } z(t)>0. \end{cases} \tag{16}$$

This model is appropriate for describing SMD before deposition, i.e. during the so-called TIG-wash passes, during which the substrate is preheated typically using 3–6 passes without filler material. It is also used for representing deposition of single beads [45,35,46]. Fig. 4 shows a successful prediction of the weld pool as well as the HAZ of a single bead specimen of Ti–6Al–4V built by SMD with the double-ellipsoidal heat source model. The heat input density rate was scaled to account for the increased volume of heat deposition (due to the material layers above $y = 0$) so that the total heat input rate equals Q [15,47].

When the double-ellipsoidal model is used, accurate computation of the welding heat source vector $F_i^{I;\text{whs}}$ (Eq. (9)) requires a sufficiently fine mesh: Goldak et al. [48] suggested that approximately four quadratic elements along each axis are needed to determine the inflection of the Gaussian surface. When using linear triangular finite elements, the heat source term can be accurately represented by setting the number of integration points per element such that at least six Gauss points are used along each axis of the double ellipsoid. For example, if six elements are placed along an axis within the ellipsoid, a single Gauss point per element is required.

Time integration parameters also play an important role. The double-ellipsoidal heat source should traverse any given section in 10–20 time steps [48]. This requires the time step size to be $O\left(\frac{c_f+c_r}{nV_w}\right)$, where $n = 10 \sim 20$. For example, for typical values $c_f + c_r = 12$ mm and $V_w = 4$ mm s^{-1}, the time step must be $\Delta t = O(0.15 \sim 0.3)$ s.

With a 2-D cross-sectional model, it is possible to increase the time step as the torch moves away from the section of analysis. When the heat source is crossing this surface, i.e. $-c_f \leqslant z \leqslant c_r$, the time step is $\Delta t_{\min} = (c_f + c_r)/(nV_w)$. Once the torch has moved beyond this section, the time step can be increased to allow for faster computations. Because the deposition of each layer normally takes 2–4 min, an enormous reduction in computational effort is achieved by changing the time step in this way. If a 3-D model were used, the correct representation of the heat source would require using $\Delta t = \Delta t_{\min}$ throughout the process.

5.1. Heat source during the deposition of SMD layers

The double-ellipsoidal heat source model is not capable of reproducing the shape of the weld pool for the second, third and subsequent layers in SMD. Fig. 5 shows a macrograph of the top region of sample 22 (see Table 1) where it appears that the bottom boundary of the FZ has a convex shape and embodies about three layers, as observed in Ref. [23] in a wall of Ti–6Al–4V built by laser deposition. Indications of the predicted highest temperatures reached during the deposition of the last layer using the double-ellipsoidal model can be observed on the right-hand side of this figure. Additionally, the contour line corresponding to the liquidus temperature of Ti–6Al–4V ($T_{\text{liq}} = 1660$ °C), which can be assimilated to the bottom boundary of the FZ, is plotted. Since heat has been distributed in double-ellipsoidal volume around the arc, the T_{liq}-contour line has a concave shape that differs from observations.

To better match experimental findings, the heat input rate density is assumed to be uniformly distributed throughout the last added layer, a hypothesis consistent with Chiumenti et al. [13]. This assumption is consistent with the artificial increase of conductivity for modelling convective effects, which renders the heat distribution in the melt more uniform. The distribution along the longitudinal z axis is, however, assumed coincident with the double-ellipsoidal model so as to match the steep gradient in

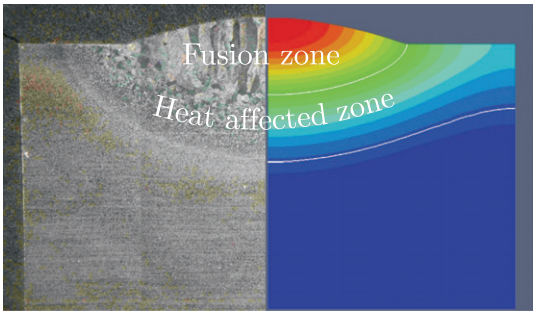

Fig. 4. Fusion zone and heat-affected zone in a single-bead specimen of Ti–6Al–4V built by SMD: macrograph vs. numerical solution using Goldak et al.'s double-ellipsoidal heat source.

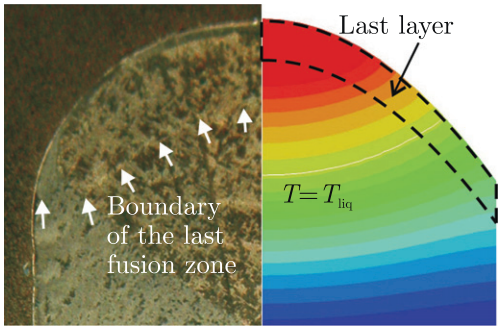

Fig. 5. Location of the boundary of the fusion zone in sample 22. On the right, maximum temperature reached during the deposition of the last layer as computed using the double-ellipsoidal heat source model [27].

the front of the welding torch and the mild decay behind the welding torch:

$$q(t_I) = \frac{\sqrt{3}Q}{\sqrt{\pi}\Omega_I^{\text{layer}}} \times \begin{cases} \frac{f_f}{c_f} \exp\left(-3\frac{z(t_I)^2}{c_f^2}\right) & \text{if } z(t_I) < 0 \\ \frac{f_r}{c_r} \exp\left(-3\frac{z(t_I)^2}{c_r^2}\right) & \text{if } z(t_I) > 0 \end{cases} \quad (17)$$

When the heat input density is assumed to be spatially uniform within the last deposited layer, the prediction of the FZ is considerably more accurate with respect to the prediction from the double-ellipsoidal model, as shown on the left of Fig. 6.

5.2. Artificial thermal conductivity for convection effects

In all heat source models proposed to date, the artificial increment of thermal conductivity to represent convection effects in the liquid phase was assumed to be isotropic:

$$\Delta\mathbf{k} = (\alpha - 1)k\ \mathbf{I} \quad (18)$$

where k is the thermal conductivity of the melt at rest and $\alpha > 1$ is a scalar. The solutions plotted in Figs. 5 and 6 (left) were computed with $\alpha = 10$.

A further improvement is achieved by realizing that heat convection occurs mainly by slipping of the molten metal in the last layer over the solidified substrate. Therefore, the artificial increment of the heat conductivity should operate mainly in this direction. We therefore define the artificial increment of the heat conductivity to account for convection effects as the orthotropic tensor:

$$\Delta\mathbf{k} = (\alpha - 1)k\ \mathbf{u} \otimes \mathbf{u} \quad (19)$$

where k and α are defined as before and $\mathbf{u}$ is the unit vector tangent to the bottom surface of the last added layer. On the right of Fig. 6, we observe the plot of computed maximum temperature. It should be noted that the T_{liq}-contour line now approaches experimental observations (Fig. 5, left).

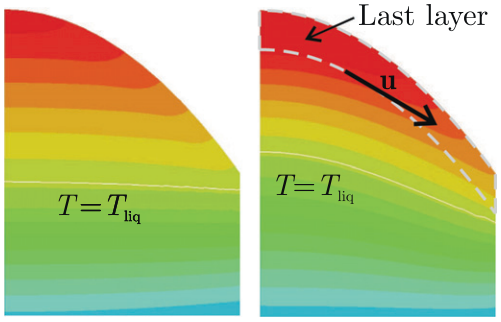

Fig. 6. Maximum temperature reached during the deposition of the final layer, computed assuming that the welding heat is uniformly distributed throughout the last added layer. On the left, the thermal conductivity is increased isotropically to represent convection effects; on the right, this increment acts only tangent to the bottom surface of the last added layer (**u** direction).

6. Application

Heat transfer is analysed for all the samples shown in Fig. 2 while assuming that heat flow is restricted to the cross-section such that a 2-D model may be used.

With Ti–6Al–4V having an average diffusivity of $4 \times 10^6 \text{m}^2\,\text{s}^{-1}$ within the welding temperature range and taking as characteristic dimension the side length (given in Table 1), the Pclet number ranges from 41.7 for sample 50 to 187.5 for samples 21–23. Because $Pe \gg 1$, the cross-sectional model is expected to be accurate enough for the purposes of this work.

The geometrical model and typical mesh for the analysis of this type of components are illustrated in Fig. 7. The temperature distribution is assumed symmetric with respect to the mid-plane of the wall; this assumption is supported by the symmetrical thermal-driven bands of the macrographs of Fig. 2.

After analysing the experimental samples we determined that the top surface of each deposited layer can be accurately described by a parabolic function; this concurs with the observations made by Wu et al. [49] on single-pass TIG beads.

Let $t_I > 0$ be the time for which the deposition of layer Ω_I^{layer} begins. At a given time t in the time interval $[t_I, t_{I+1})$, the domain of analysis is $\Omega_I = \Omega_0 \cup \Omega_1^{\text{layer}} \cup \ldots \Omega_I^{\text{layer}}$, where Ω_0 denotes the substrate sub-domain, coincident with the entire domain at $t_0 = 0$. The mesh should be constructed such that the fact that the domain is subdivided into layers (subdomains) is accounted for, as shown in Fig. 7.

Let Γ_I be the boundary of Ω_I, consisting of a portion Γ_I^{sym} laying on the symmetry axis, and hence adiabatic,

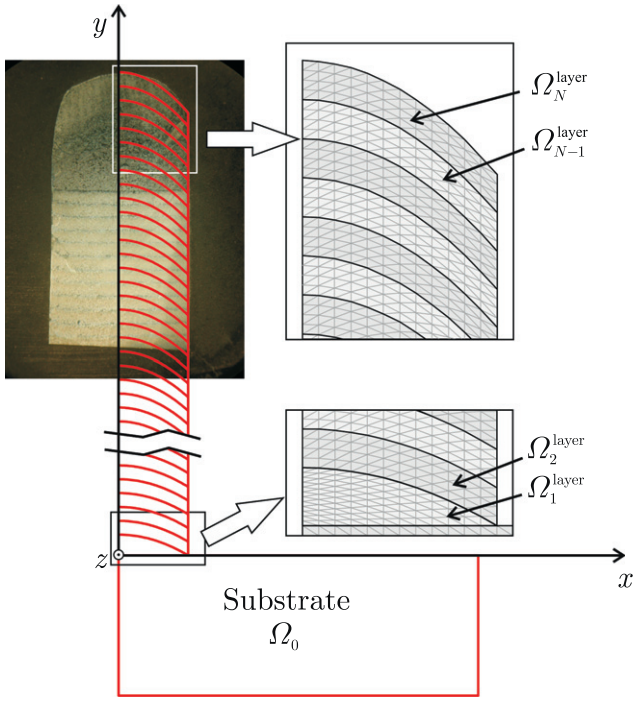

Fig. 7. Geometrical model for the analysis of sample 24.

and a portion Ω_I^{cr} through which the piece exchanges heat with the environment (the sealed argon-filled chamber) by combined convection and radiation, such that $\Gamma_I = \Gamma_I^{sym} \cup \Gamma_I^{cr}$ and $\Gamma_I^{sym} \cap \Gamma_I^{cr} = \emptyset$. The boundary conditions of the problem should be defined to be evolving in time following the addition of layers.

A minimum time step of $O(0.1\ s)$ is used for tracking the highly concentrated welding heat source with sufficient accuracy while the heat source is traversing the section of analysis. The time step is increased smoothly from this value as the torch leaves, reaching a maximum value ($O(1-10\ s)$, depending on the duration of each pass) when the torch is farthest away. After this moment, it decreases smoothly until the studied section is reached again.

The welding heat source, as given by Eq. (16) during TIG-wash and the deposition of the first layer or by Eq. (17) after that, is defined assuming a equals half the thickness of the bead, $c_f = b = a$, $c_r = 4c_f$, $f_f = 2c_f/(c_f + c_r) = 2 - f_r$ and the total heat input in arc welding is given by $Q = \eta V A$, where V and A are the voltage and amperage listed in Table 1, and η is the efficiency of the arc, assumed to be equal to 0.7. Temperature-dependent material data for Ti–6Al–4V were taken from Ref. [50].

As suggested by several authors [27,35,51–53], combined convection and radiation are prescribed as boundary conditions, thereby defining a convection-radiation heat transfer coefficient:

$$h_{cr} = 2.41 \times 10^{-4} \varepsilon T^{1.61} \tag{20}$$

where h_{cr} is given in $W\,m^{-2}\,K^{-1}$ for T given in K, and $\varepsilon = 0.9$ is the surface emissivity.

We aim to determine the size of the top region, which is defined as the region where the peak temperature exceeded the β-transus $T_\beta \approx 1000\ °C$ during the last welding pass. To this end, the map of the maximal temperature attained during the deposition of the last layer inside the whole domain is determined. The contour curve corresponding to T_β in this map defines the interface between the top and the bottom region.

Fig. 8 shows the location of this interface for all of the studied samples. Numerical results fit qualitatively and quantitatively well to what is observed in macrographs. This figure indicates that the SMD parameters have a complex influence on the height of the top region. The model has been able to predict this region with accuracy.

Several authors have reported that the HAZ for current-pulsed or spot TIG welding of Ti–6Al–4V has a mainly martensitic microstructure due to the high cooling rates [28–30]. However, we did not observe a considerable amount of martensite in SMD of Ti–6Al–4V [2], or in robotized TIG metal-wire deposition (RTMwD) of Ti–6Al–4V [54,55]. According to Ahmed and Rack [56], partial transformation of α phase into martensite α' takes place for cooling rates between 20 and 410 $°C\,s^{-1}$ (both measured at 900 °C). High cooling rates are observed at 900 °C through the HAZ after the deposition of the first layer in SMD (Fig. 9a). However, this zone is reheated above 1000 °C and then tempered when the next layer is added (Fig. 9b). Note also that during the deposition of the last layer, the cooling rate is sensibly lower than that attained when the first layer was added (Fig. 9c). Although the wall does not suffer any other reheating after deposition of the final layer, the low cooling rate attained at the end of the process suggests that very little martensite may form in this zone and that it may not be visible in macrographs. This explains why the microstructure observed in SMD-built Ti–6Al–4V components

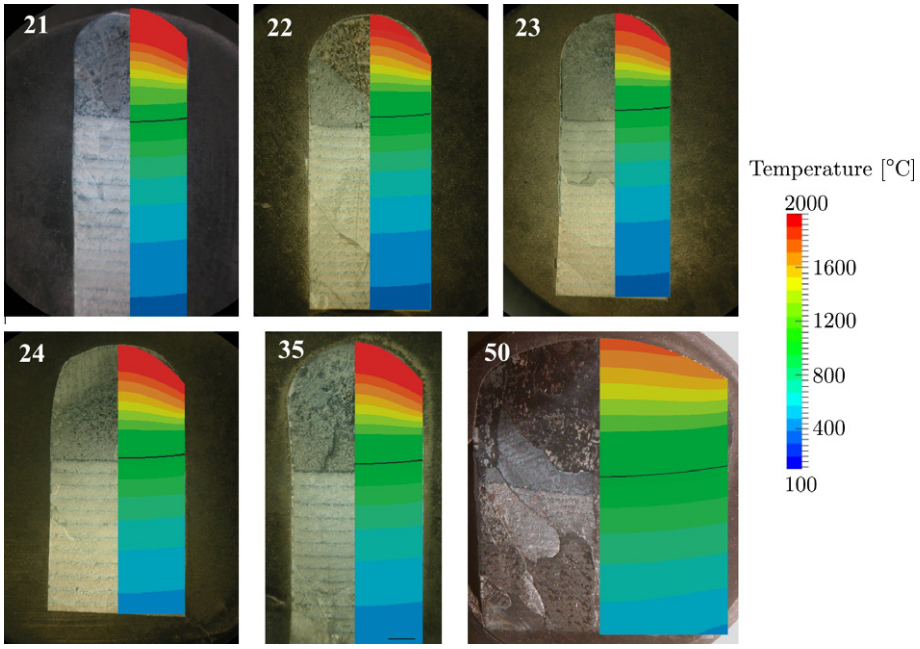

Fig. 8. On the right side of each sample, the maximal temperature attained during the deposition of the final layer, where β-transus contour is highlighted.

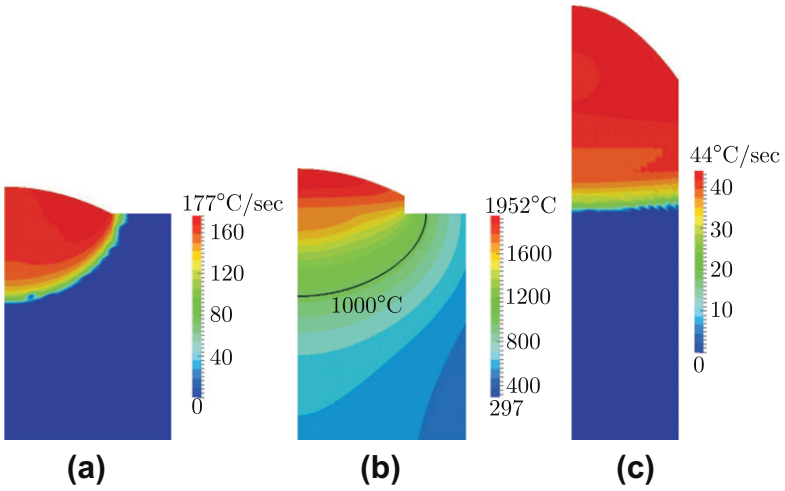

Fig. 9. Cooling rate and temperature in sample 22: (a) cooling rate at 900 °C during the deposition of the first layer; (b) maximal temperatures attained during the deposition of the second layer; (c) cooling rate at 900 °C during the deposition of the first layer.

differs from that observed in spot or current-pulsed TIG welding of the same alloy.

7. Conclusions

This paper presents a thermal-microstructural model that explains the complex thermal phenomena that take place in the SMD process with an emphasis on the successful prediction of the extent of the top region. The model is 2-D for accuracy and efficiency reasons: a fine spatial mesh can be used and the entire interval of interest (2–3 h) can be modelled using a fine time step (0.1 s) when needed.

The numerical model predicted that melt sliding on the previously deposited material is an important means of heat transfer that cannot be neglected. This effect was simulated using an artificially increased orthotropic conductivity along the transversal sliding direction.

Several important microstructural features in the produced components were explained by the model, allowing the observed final microstructure to be related to the temperature history at each point. The model correctly predicted the shape and extent of a top cupola with a particular microstructure different from the layers below, the absence of martensite, and the typically layered microstructure produced by cooling and reheating of a SMD-built component.

Acknowledgements

The support from European Community, contract AST 5-CT 2006-030953, project RAPOLAC (Rapid Production of Large Aerospace Components) of the 6th Framework Programme of the European Commission (www.RAPOLAC.eu), CONICET (Consejo Nacional de Investigaciones Científicas y Técnicas, Argentina), and UNL (Universidad Nacional del Litoral, Argentina) is gratefully acknowledged.

References

[1] Bishop J. Shaped metal deposition apparatus. US patent application 20100251961, Rolls-Royce plc, London; 2010.
[2] Baufeld B, Van der Biest O, Gault R. Int J Mater Res 2011;11:1536–42. http://dx.doi.org/10.3139/146.110217.
[3] Goldak J, Akhlaghi M. Computational welding mechanics. Springer Science+Business Media, Inc; 2005.
[4] Lindgren LE. Computational welding mechanics. Thermomechanical and microstructural simulations. Woodhead Publishing Ltd; 2007.
[5] Dalhuijsen AJ, Segal A. Int J Numer Methods Eng 1986;23:1807–29.
[6] Voller VR, Swaminathan CR, Thomas BG. Int J Numer Methods Eng 1990;30:875–98.
[7] Tamma KK, Namburu RR. Int J Numer Methods Eng 1990;29:1473–85.
[8] Yao M, Chait A. Metall Trans B 1993;24:279–300.
[9] Fachinotti VD, Cardona A, Huespe AE. Int J Numer Methods Eng 1999;44:1863–84.
[10] Costa L, Vilar R, Reti T, Deus A. Acta Mater 2005;53:3987–99.
[11] Longuet A, Colin C, Peyre P, Quilici S, Cailletaud G. Modélisation de la fabrication directe de pièces par projection laser: application au Ti–6Al–4V. In: Matériaux 2006, Dijon, France; 2006.
[12] Longuet A, Robert Y, Aeby-Gautier E, Appolaire B, Mariage JF, Colin C, et al. Comput Mater Sci 2009;46:761–6.
[13] Chiumenti M, Cervera M, Salmi A, Agelet de Saracibar C, Dialami N, Matsui K. Comput Methods Appl Mech Eng 2010;199:2343–59.
[14] Lundbäck A, Lindgren L. Finite Elem Anal Des 2011;47:1169–77.
[15] Anca A, Fachinotti VD, Escobar-Palafox G, Cardona A. Int J Numer Methods Eng 2011;85(1):84–106.
[16] Fachinotti VD, Anca AA, Cardona A. Int J Numer Methods Biomed Eng 2011;27:595–607.
[17] Wahab MA, Painter MJ, Davies MH. J Mater Process Technol 1998;77:233–9.
[18] Ferro P, Porzner H, Tiziani A, Bonollo F. Model Simulat Mater Sci Eng 2006;14:117–36.
[19] Abid M, Siddique M. Int J Pres Ves Pip 2005;82:860–71.
[20] Edstorp M. Weld pool simulations. Licentiate thesis. Department of Mathematical Sciences, Chalmers University of Technology and University of Gothenburg, Sweden; 2008.
[21] Barsoum Z, Lundbäck A. Eng Fail Anal 2009;16:2281–9.
[22] Lindgren LE. Comput Methods Appl Mech Eng 2006;195:6710–36.
[23] Kelly SM. Thermal and microstructure modeling of metal deposition processes with application to Ti–6Al–4V. PhD thesis. Virginia Polytechic Institute and State University; 2004.

[24] Kelly SM, Kampe SL. Metall Mater Trans A 2004;35:1869–79.
[25] Charles C, Järvstråt N. Modelling Ti–6Al–4V microstructure by evolution laws implemented as finite element subroutines: application to TIG metal deposition. In: David SA, DebRoy T, DuPont JN, Koseki T, Smartt HB, editors. Proceedings of the 8th international conference trends in welding research; 2009, p. 477–85.
[26] Baufeld B, Van der Biest O. Sci Technol Adv Mater 2009;10. doi:10.1088/1468-6996/10/1/015008..
[27] Goldak J, Chakravarti A, Bibby M. Metall Trans B 1984;15:299–305.
[28] Elmer JW, Palmer TA. J Appl Phys 2004;95(12):8327–39.
[29] Babu NK, Raman SGS, Mythili R, Saroja S. Mater Charact 2007;58:581–7.
[30] Balasubramanian M, Jayabalan V, Balasubramanian V. Mater Lett 2008;62:1102–6.
[31] Rai R, Elmer JW, Palmer TA, DebRoy T. J Phys D: Appl Phys 2007;40:5753–66.
[32] Kelly SM. Characterization and thermal modeling of laser formed Ti–6Al–4V. Master's thesis. Virginia Polytechnic Institute and State University; 2002.
[33] Robert Y. Simulation numérique du soudage du TA6V par laser YAG impulsionnel: caractérisation expérimentale et modélisation des aspects thermomécanique associées à ce procédé. PhD thesis. Ecole des Mines de Paris; 2007.
[34] Dike JJ, Ortega AR, Rangaswamy P. Finite element modeling and validation of residual stresses in 304l girth welds. In: 5th International conference on trends in welding research, Pine Mountain, GA; 1998.
[35] Bonifaz EA. Weld Res 2000;(Suppl. May):121–5.
[36] Ericsson M. Simulation of robotic tig-welding. Licentiate thesis. Department of Technology, University of Trollhättan/Uddevalla, Sweden; 2003.
[37] Yeh RH, Liaw SP, Yu HB. J Mar Sci Technol 2003;11(4):213–20.
[38] Zhang W, Kim CH, DebRoy T. J Appl Phys 2004;95(9):5220–9.
[39] Zhuk HV, Kobryn PA, Semiatin SL. J Mater Process Technol 2007;190:387–92.
[40] Mufti RA. Mechanical and microstructure investigation of weld based rapid prototyping. PhD thesis. Ghulam Ishaq Khan Institute of Engineering Sciences and Technology Session, Pakistan; 2008.
[41] Askari A, Das S. J Mater Process Technol 2006;173:1–13.
[42] Zienkiewicz OC, Taylor RL. The finite element method. Volume 1: The basis, 5th ed.. Butterworth-Heinemann; 2000.
[43] Nguyen NT, Ohta A, Matsuoka K, Susuki N, Maeda Y. Weld Res 1999;(Suppl. August):265–74.
[44] Mendez, P.F. Joining metals using semi-solid slurries. Master's thesis, Massachusetts Institute of Technology; 1995.
[45] Carmignani C, Mares R, Toselli G. Comput Methods Appl Mech Eng 1999;179:197–214.
[46] Bate SK, Charles R, Everett D, OGara D, Warren A, Yellowlees S. Sensitivity of predicted residual stresses to modelling assumptions. In: Youtsos AG, editor. Residual stress and its effects on fatigue and fracture. Springer; 2006. p. 105–15.
[47] Anca A, Cardona A, Risso J, Fachinotti VD. Appl Math Model 2011;35(35):688–707.
[48] Goldak J, Bibby M, Moore J, House R, Patel B. Metall Trans B 1985;17:587–600.
[49] Wu CS, Chen J, Zhang YM. Comput Mater Sci 2007;39(3):635–42.
[50] JAHM Software, Inc,. MPDB v7.37. 2011.
[51] Fan HG, Kovacevic R. J Phys D: Appl Phys 2004;37:2531–44.
[52] Wu CS, Zhao PC, Zhang YM. Weld Res 2004:330–5.
[53] Wu CS, Fan F. Model Simulat Mater Sci Eng 2004;12:13–20.
[54] Charles C, Järvstråt N. Development of a microstructure model for metal deposition of titanium alloy Ti–6Al–4V. In: Proceedings of the 11th world conference on titanium (Ti-2007), Kyoto, Japan; 2007.
[55] Charles Murgau C, Pederson R, Lindgren LE. Model Simulat Mater Sci Eng 2012;20:055006.
[56] Ahmed T, Rack HJ. Mater Sci Eng A 1998;243:206–11.